

Preliminary report on master project

Rikesh Chauhan

1 Introduction

This report is a brief overview of my master project on wireless power transfer through inductive coupling. It is the documentation of the schematic of complete design of the power receiving unit. It includes brief explanation about choices of design topologies and techniques. Figure 1 is the block diagram of the complete design including the test PCB and the test chip on it.



Figure 1: Block diagram of complete design

As shown in the block diagram above, the design includes antennas rectifier, LDO regulator and reference and biasing circuits. This report mainly discusses about the various design aspect of rectifier and LDO. The inductor is designed with the specifications provided by NORDIC. The biasing and reference circuit is designed solely for learning the design technique without much effort on the accuracy of the generated biases and references. So externally supplied bias and reference will

be the secondary option. The project is designed in tsmc90nm process. Table 1 lists the main specifications of this project.

Table 1: Project specifications

Technology	TSMC 90nm 9M-1P
Chip area	TBA mm ²
Input AC voltage	2.5 V _p
Operating frequency	13.56 MHz
Maximum load	10 mA
Output DC voltage	1.8 V

A brief discussion of rectifier design is followed next.

1.1 Motivation

The ongoing modern technological advancements have led us into dramatic and drastic electronic device development trend. On the one hand devices are getting smaller, lighter and low-powered, while on the other hand more and more functionality with increased speed are being integrated. And above all these, going wireless whenever and whatever possible is the market trend. Specially in commercial electronics, it looks like quest for the ultimate gadget, miniaturised low-powered multi-functional wireless device, is not going to stop anytime soon. Thanks to non-stop research and development in manufacturing, material and technology.

1.1.1 Technology Trend

Reduction in size and weight has been most dramatic that in course of some decades miniaturisation trend went from a room-sized fixed electronic into a wearable device. Most important milestone contributing for lighter and tighter devices is development of transistor in Bell Lab in 1950s replacing large and bulky vacuum tubes. Similarly development first integrated circuit, IC, in 1965 added another stepping stone towards miniaturisation of electronic device, making it possible to integrated hundreds of transistors on a single silicon substrate of some square mm. Since then as stated by Moore's law, IC size is continuously shrinking. A typical modern IC now consists of billions of transistors of some tens of nm feature size.

On the contrary to shrinking device size, integrated functionality and device speed is increasing proportionally. The introduction of SoCs created of new dawn of multi-functionality IC by integrating many electronic components and/or systems on a single silicon substrate. Similarly multi-core CPU with parallel programmed instruction significantly increased work payload as stated by Amdahl's law. Similarly recent developments in IoT has introduced whole new dimension on multi-functionality by connecting many devices to a same local network or the internet[1].

In terms of power consumption, though power density has increased due to increased transistor density and speed, power consumption per transistor and energy per operation, EOP, has significantly reduced.

It is due to gradual shrinking in feature size and decrease in supply voltage. Similarly there has been a lot progress in LP design introducing new power optimal design techniques both at logic/circuit level and architecture level. Lately run time power optimisation technique by tracing realtime work load like dynamic voltage scaling and switching between different operation modes (sleep, nap, doze and active) have been popularly used to reduce power consumption[2].

In spite of dramatic technological advancement batteries are still used as power source to drive electronics devices. It is not like there has been no progress in battery technology. There has been a lot improvements like increased volumetric energy density thereby reducing size, increased gravimetric energy density thereby reducing weight, reduced self discharge thereby increasing life time and increased charged cycle thereby increasing reuse.[CITE]. Today Li-ion has better choice for powering devices because of it better combined above mentioned characteristics.

Though there has been progress in battery technology, use of battery in todays' handheld and portable devices have disadvantages. Batteries contribute significant proportion of total weight and size of the device. They occupy more space, require regular recharge and in the long run need replacement. WPT helps to overcome some of these limitations. For example instead of removing and recharging batteries, they can be recharged with harvested energy without removing them. Going one step further ahead, batteries can be completely replaced in a electronic device and power the device wirelessly. This way implementation of WPT helps to minimise the problems of battery powered device and in the best case completely removes the problems.

1.2 Energy Harvesting

Today many different energy harvesting techniques have been studied and implemented. There has been tremendous success in harvesting low power from ambient sources and a lot of effort and resources is being used for harvesting high power. As discussed earlier the technological advancement has given us low power electronics. These LP devices can now be powered solely by harvested energy, eventually making battery-less wirelessly powered electronic device a reality.

Energy harvesting system generally constitutes of energy source, transducer and power conditioning unit. Energy source can either be artificial like human walking or natural like sunlight. Transducer are devices which converts the energy from source which may be to electrical energy. And power conditioning unit process the harvested energy so that it can be used either to directly power a load or to store the energy.

Depending upon the type of energy harvested from the surrounding environment, energy harvesting devices can be broadly classified into kinetic, electromagnetic and thermal energy sources[3]. In kinetic energy harvesting, kinetic energy due to mechanical deformation of transducer is converted into electrical energy. Piezoelectrical material is good example of transducer for kinetic energy harvesting. Piezoelectrical materials are those which exhibit piezoelectric effect: when subjected to mechanical strain, it generates electrical charge proportional to applied strain. Strain is applied with either compression, slap or bending of the material.

Electromagnetic energy harvesting is extraction of useful energy from ambient light or RF radiation. Solar energy harvesting is the most popular and widely successful EM energy harvesting for large scale energy generation. It makes use of semiconductor device called solar cells as transducer. These transducer converts incident light energy to electric energy due to photoelectric effect: when light is incident on semiconductor, electrons are emitted from the surface. Its application ranges from LP wrist watch to grid of photovoltaic system. The other popular example is harvesting from ISM RF radiation, which are available almost everywhere in modern cities, to power RFIDs. In this technique, antenna or rectenna are used as transducer. However harvesting from ISM radiation has been limited to very low power only.

Similarly in thermal energy harvesting, thermal energy from any source in the environment is converted to useful electric energy. Thermopile is an example of thermal energy harvesting using thermocouples in series as transducer. Thermocouple is a electric device with two different conductors forming junctions. A thermocouple generates voltage proportional to temperature between junctions, known as Seebeck effect. Connecting thermocouples in series increased the harvested voltage as in thermopile.

Though it has discussed above about powering micro-electronics devices with harvested energy from ambient sources, the reality with commercial micro-electronic device is a different story. Very low power and some low power micro-electronic only have the privilege of integrating energy harvesting techniques so far. It is still limited to research and development phase for moderate to high power harvesting for micro electronic devices. If we observe the trend of technology development in reducing power consumption of micro devices and at the same time, the progress in R&D with promising results in power harvesting, we can definitely expect that harvested power will meet power requirement of electronic devices in near future. But consumers' desire for battery-less and wireless electronics has made the commercial electronics producers to make most use of latest advancements. This has led to integration of latest development with already matured technology for the sake of consumers' satisfaction and for bigger share of the market. And hence wireless power transfer has gained much popularity.

1.3 Wireless Power Transfer

2 Rectifier

The most basic rectifier is conventional full wave bridge structure where the diodes are replaced by the diode connected MOS. devices in CMOS. technology. This topology though being simple to implement, has a major drawback. It requires at least twice the V_{tn} of a MOS device as there are two diode connected MOSes in the conduction path for each cycle of the input signal.

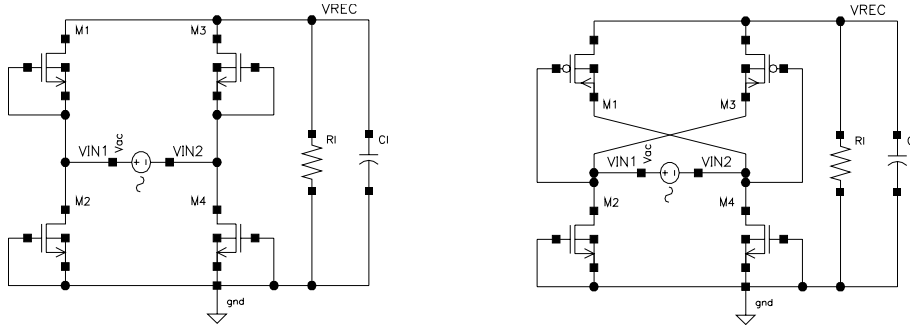
Gate cross coupled and fully gate cross coupled topologies are improvements over conventional full wave rectifier. In gate cross coupled rectifier, two diodes of conventional rectifier is replaced by two gate cross coupled MOSes working as switches where the voltage drop for every cycle is reduced to one threshold voltage. Similarly, in the fully gate cross coupled rectifier, all diodes are replaced by switches and hence the voltage drop is further reduced to twice the conduction drop only for every cycle. Even though this topology has least voltage drop, it suffers from the problem of reverse charge leakage because when the input ac amplitude is less than the output rectified voltage and the conducting pass devices are on simultaneously, current flows backward from output to input.

All the above discussed topology suffer from either large voltage drop or large power loss because of which their use are limited in low power and low voltage devices. The popular techniques for higher efficiency are using gate cross coupled rectifier along with passive or active circuitry for controlling other two pass devices. In passive rectifier, additional circuitry including bootstrap capacitor are used to reduce or eliminate threshold voltage one of which is discussed in this paper [4]. However, use of on-chip bootstrap capacitors limits its use where chip area and speed is of importance. On the other hand, in active rectifier, active circuitry is used to control pass devices. The use of active circuitry increases both voltage conversion efficiency (VCE) and power conversion efficiency (PCE) because the pass devices are made to conduct in linear region and hence less conduction drop, and reverse current flow can be completely eliminated and hence less power loss. However active rectifier is not problem free either. The major issue is starting of the active circuit as there is no regulated supply at the start up.

2.1 Design

In this project, active rectifier is chosen, primarily for better VCE and PCE and secondarily to avoid the use large on chip capacitors. [5] and [6] have discussed same active rectifier topology with a slight difference in active circuitry. [5] has implemented comparator with compensating the delay of comparator's output falling whereas [6] has implemented comparator with compensating both the falling and the rising delay of comparator's output in expense of added circuit complexity and power consumption. [5] has been used here for its simple design.

Figure 2a, 2b and 3 is the CMOS implementation of conventional full wave bridge rectifier, gate cross coupled rectifier and proposed active rectifier in [5]. The problem with 2a and 2b has already been briefly mentioned above. Though 2b is significantly improvement over 2a, it is still not a favourable topology with respect to the design technology chosen. In the gate cross couple rectifier of 2b, the cross coupled pMOSes act as switches, so the only voltage drop across them is conduction drop due to channel resistance. However the other two nMOSes are diode connected, so they have at least V_{tn} drop across them which means $V_{ac} \geq V_{dc} + V_{tn}$ for conduction.



(a) Conventional full wave bridge rectifier (b) Gate cross coupled full wave rectifier

Figure 2: Rectifier topologies: conventional and gate cross coupled

The proposed active circuit in 3 is improvement over 2b which eliminates V_{tn} drop required for conduction by replacing diode connected nMOS with devices controlled by active circuit as shown in figure 4. The active circuit is a four input comparator that turns on nMOSes fast when $V_{ac} > V_{dc}$ and turns off fast to avoid flow of current.

For the illustration of operation of comparator, consider the case when $V_{in1} > V_{in2}$ i.e. $V_{in1} > 0$ and $V_{in2} < 0$. During this half cycle, comparator $D1$ output is low and turns off M_{n2} and also, M_{p1} is reversed biased and hence there is no path to flow current along M_{n2} and M_{p1} . For simplicity, assume $V_{ac} = V_{in1} - V_{in2}$. When V_{ac} reaches V_{tp} , M_{p3} turns on which shorts V_{in1} to V_{rec} . When $V_{ac} > V_{rec}$, $D2$ output goes high, which turns on M_{n4} and starts the conduction path for the first half cycle and starts charging C_l . When V_{ac} reaches maximum, it starts to decrease and at $V_{ac} < V_{rec}$, conduction stops as output of $D2$ is low and M_{n4} is off. As V_{ac} further decreases to below V_{tp} , M_{p3} if off too. This way rectifier in 3 conducts during positive half cycle eliminating the V_{tn} drop seen in 2b. Now the only drop is the conduction drop due to channel resistance of two pass devices along the conduction path. This drop is much less because during conduction both the device are operating in the linear region with small resistance. The operation is similar for $V_{in2} > V_{in1}$ where M_{n4} and M_{p3} are off and M_{n2} and M_{p1} conduct to charge C_l .

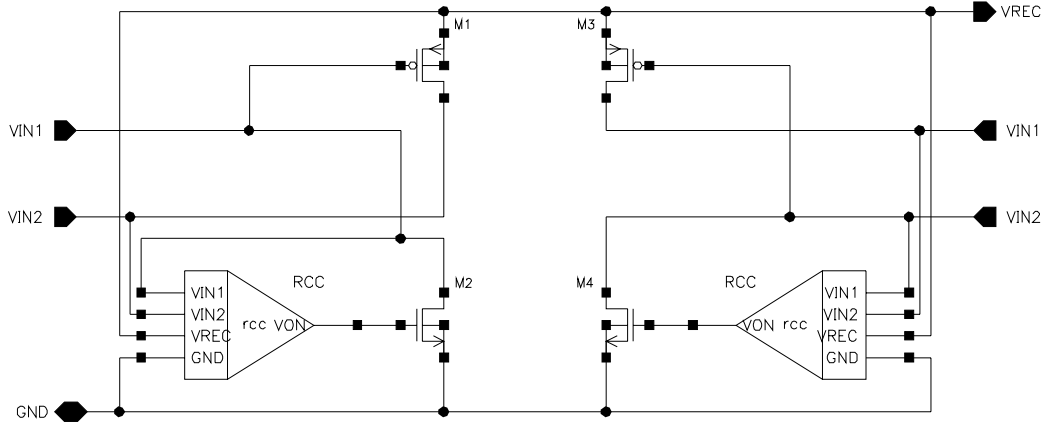


Figure 3: Gate cross coupled full wave active rectifier]

Figure 4 is the implementation of four input comparator $D2$ used in 3 as proposed in [5]. It is designed to self power and bias because no steady state supply is available at start up. $M1$, $M2$ and $M7$ monitors voltage across M_{n4} i.e $V_{in2} - V_{gnd}$ and $M3$, $M4$ and $M8$ monitors voltage across M_{p3} i.e $V_{in1} - V_{rec}$. So when $V_{in1} - V_{rec} > V_{in2} - V_{gnd}$ which means $V_{ac} > V_{rec}$, output of $D2$ is high and turns on M_{n4} instantly. But when $V_{ac} < V_{rec}$, the output of comparator is delayed to

fact that RCC is self powered and LDO which will follow this rectifier will be powered by V_{rec} . Similarly, the value of ripple rejection capacitor is chosen 100nF. This size of filter capacitor is calculated from capacitor current-voltage relationship with the assumption of keeping peak to peak ripple voltage below 5 mV to deliver 11 mA current.

Table 2: Rectifier design parameters

Wn/Ln, Wp/Lp	720um/280nm, 1.2mm/280nm
Rectifier area	TBA mm ²
Operating frequency	13.56 MHz
Input ac magnitude	2.5 V _p
Load current	11 mA
Ripple rejection capacitor	100 nF

2.2 Transient performance

Figure 5 is the test bench setup for simulation of the rectifier. Figure 6 show the simulation results showing voltages at the input ac and output rectified DC voltages and current through rectifying MOSes. These waveforms clearly follows the working principle discussed above. Two important observations can be made from plots. First, the rectified output V_{rec} is 2.2 V for V_{pp} ac input of 2.5 V for driving which means the voltage loss has been significantly reduced and the loss of around 300 mV yields to the conduction loss due the channel resistance. Secondly, the reverse current from output to input has been effectively eliminated as there is only positive current flowing to the load when all conducting devices are on.

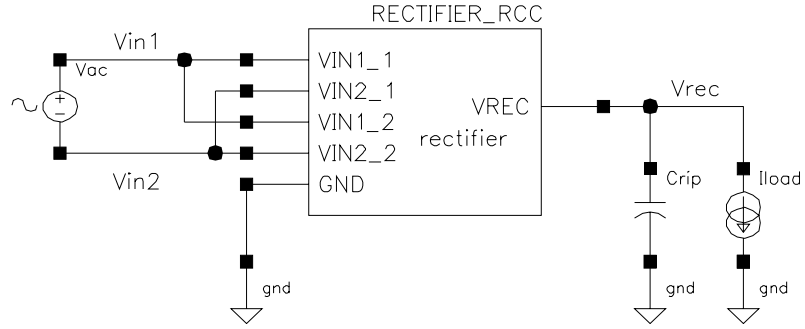


Figure 5: Testbench for rectifier

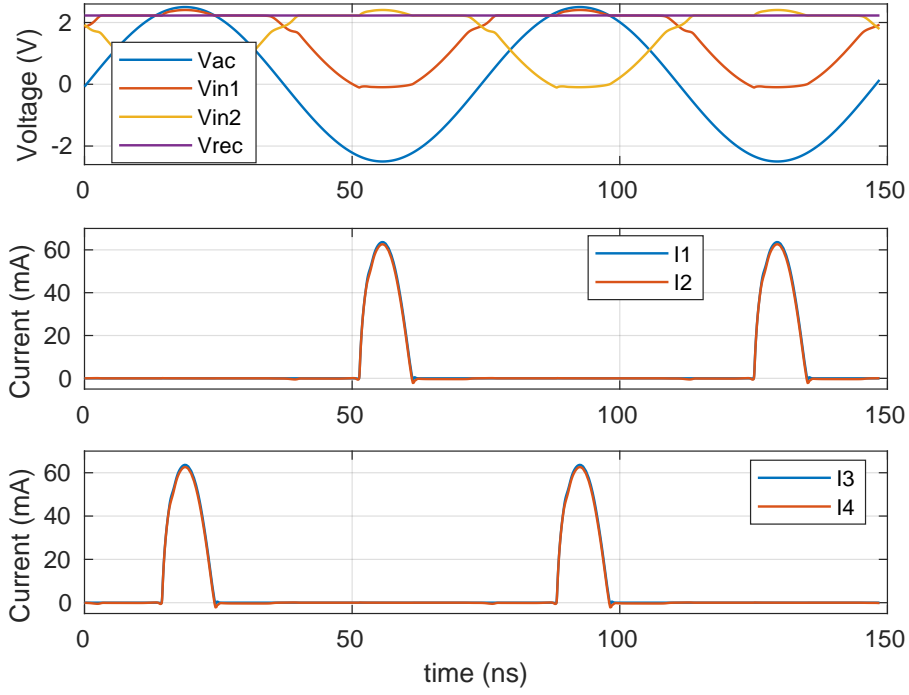


Figure 6: Voltage and current waveforms of the rectifier

Figure 7 presents both pre and post layout results of input voltages, V_{in1} and V_{in2} and output voltage, V_{rec} , for one cycle of ac input. The closer view of rectified output is shown in figure 8. The voltage drop of about 60 mV in layout result is accounted for the voltage drop due to the resistance of high current conduction path.

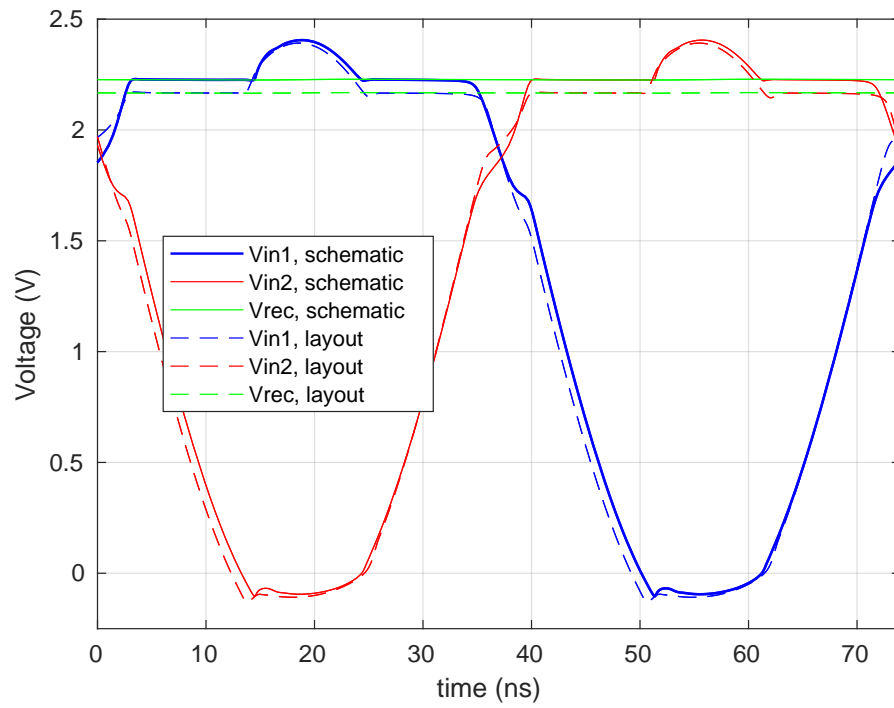


Figure 7: Voltages waveform for pre and post layout

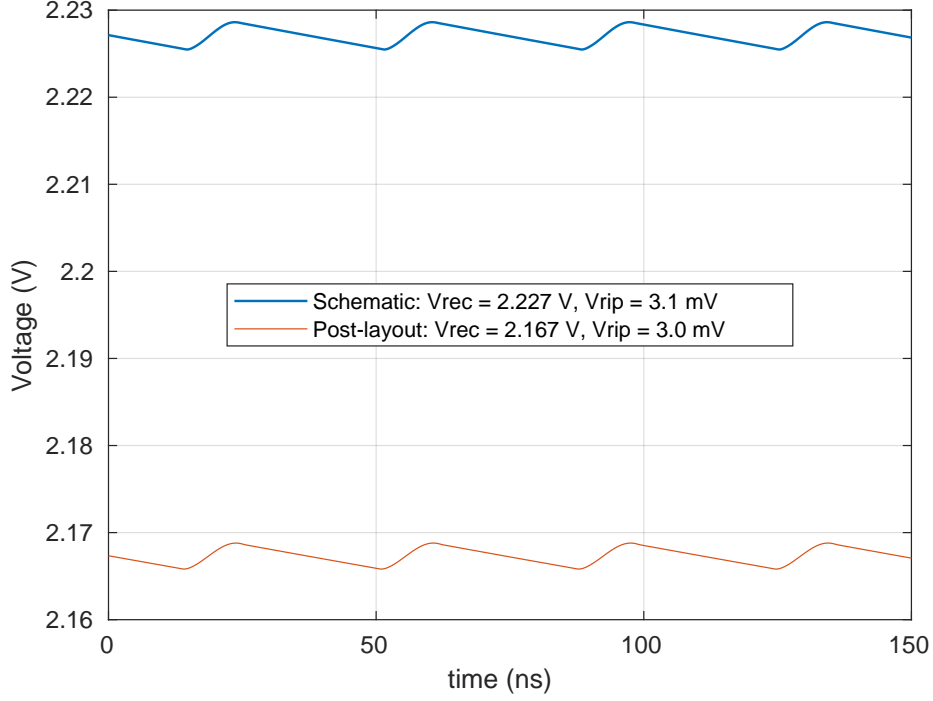


Figure 8: Rectified DC output for pre and post layout

2.3 DC performance

Similarly, figure 9 shows PCE, ratio of powered delivered to load to average power from the source and VCE, ratio of rectified DC, V_{rec} to peak ac input, $|V_{ac}|$ with respect to magnitude peak ac input signal. $|V_{ac}|$ is gradually increased in peak magnitude in step of 50 mV and VCE and PCE is calculated for every step. The plot shows both PCE and VCE are very less for input ac amplitude less than 1.8 V. It can be explained by the fact that required bias current and gate drive voltage for RCC circuit are not achieved for smaller input. [INCLUDE POST LAYOUT RESULT TOO]

Table 3 comparatively summarises performance for pre and post layout result of the design. The layout design is attached in appendix. The layout is made symmetrical with four inputs, as seen in test bench figure 5, instead of two. This is done to make the current conducting path equal which result in equal drop in voltage when it reaches the rectifying MOSes. Similarly the paths from the pad to the recti-

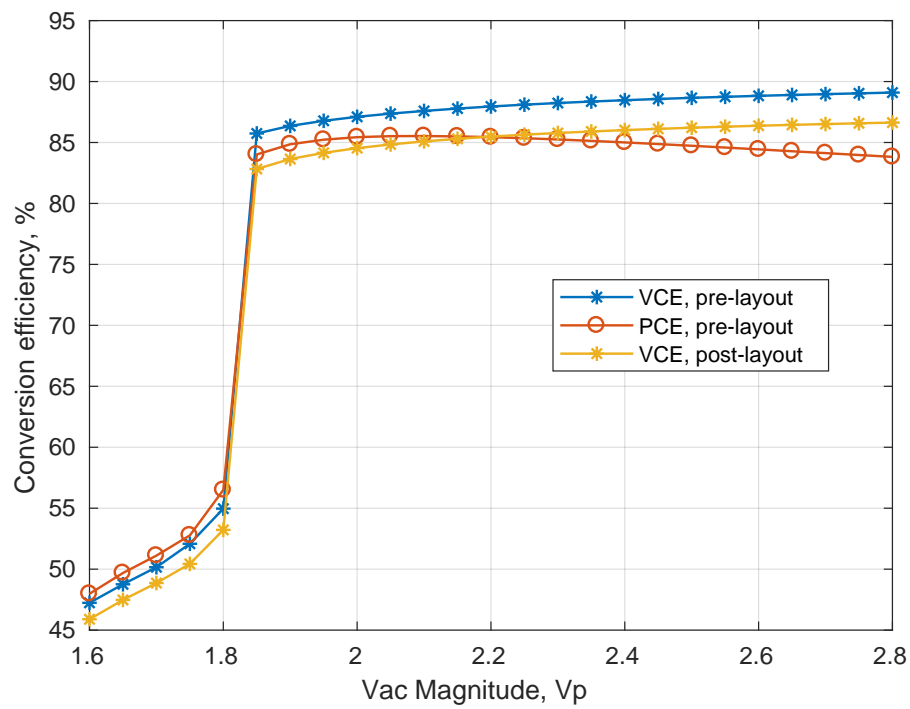


Figure 9: Voltage and power conversion efficiency

fier inputs are mask blocked for random metal fill to avoid inter layer coupling [WHY???]. The high current conduction routes are designed with wide parallel path of many higher level metal layers for reducing resistance in conduction path.

Table 3: Rectifier performance summary

	Schematic	Post-layout
Rectified DC	2.23 V	2.17 V
Ripple Vpp	3.1 mV	3 mV
Peak diode current	63.7 mA	-
PCE	84.5 %	-
VCE	88.6 %	86.2 %

3 LDO

Voltage regulator follows the rectifier designed above in order to regulated the rectified voltage to 1.8 V and deliver maximum load current of 10 mA. Since the output from the active rectifier is 2.2 V and the required regulated voltage is 1.8 V, charge pump or SMPS of boost type is irrelevant here. Buck SMPS could be an option for voltage regulation but LDO is preferred for it better performance in terms of noise and faster settling of regulated voltage. [8].

Figure 10 shows a circuit of typical LDO with pMOS as pass element. As shown in the figure, the components includes an error amplifier (EA), a pass device (Mpass), a feedback circuit (R1 and R2) and load (C_{out} and I_{load}). A more general and complete LDO circuit also includes circuitry for generation of reference voltage and bias current/voltage. In this project it will be discussed separately later. The working principle of LDO is that the error amplifier compares the scaled down regulated voltage, V_{div} with V_{ref} and regulates the internal resistance of the pass transistor such that the error, $V_{ref} - V_{div}$ is least or zero ideally.

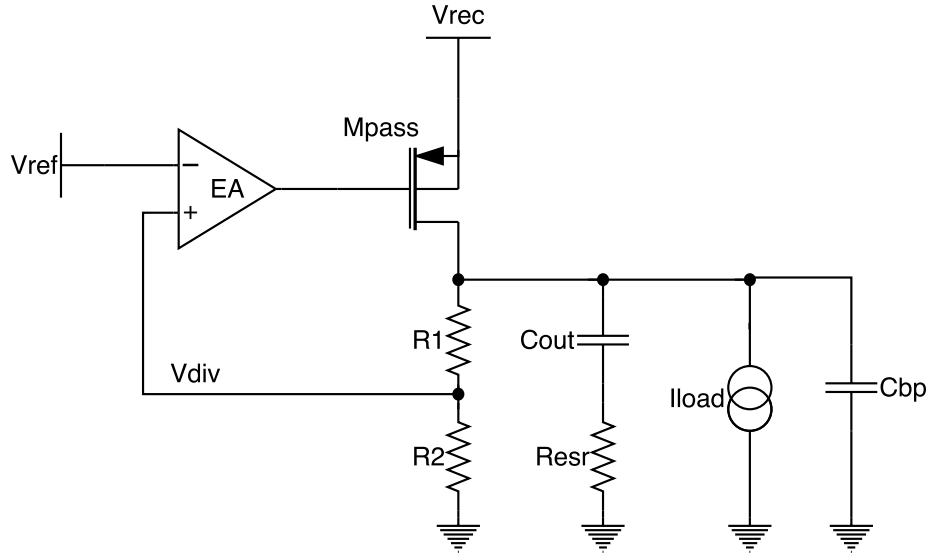


Figure 10: Generic LDO with pMOS pass device

[9] and [10] are two examples of CMOS implementation of LDO. [9] has proposed bulk modulation technique for improving load regulation and stability of capacitor-less LDO. Similarly [10] has proposed tech-

niques for increasing current efficiency of LDO especially at no or low load condition. Though the techniques discussed in these designs have not been used, they have given good insight into different design parameters of LDO.

3.1 Design

Figure 11 shows the CMOS implementation of LDO in this project. The components in this design include a folded cascode differential amplifier as error amplifier, pMOS buffer, pMOS pass device and feedback network of resistors.

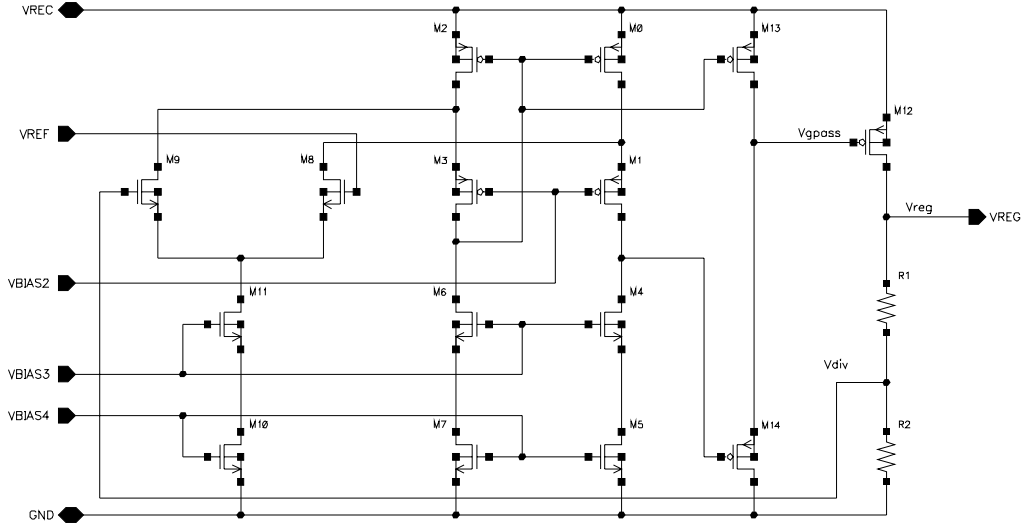


Figure 11: CMOS implementation of LDO

As briefly mentioned above, the error amplifier amplifies the error i.e. difference in scaled regulated voltage, V_{div} and reference voltage, V_{ref} . It is known that an amplifier with higher open loop DC gain reduces the closed loop gain error and hence amplifier with higher gain is desired here which in turn increases the accuracy of regulated voltage, V_{reg} [9]. Typically error amplifier has gain $> 40dB$ which is not achieved with a single stage amplifier with this technology. Higher gain can be achieved by cascading multiple single stage but with increased difficulty in making the multistage amplifier stable. So for achieving higher DC gain and at the same time for stability conveni-

ence, folded cascode amplifier [11, pp. xx] is chosen.

Table 4: LDO design parameters

Pass device	pMOS
$(Wp/Lp)_{\text{pass}}$	540um/280nm
Input supply	>2.2 V
Error amplifier	folded cascode
Vbias2	1.1 V
Vbias3	0.88 V
Vbias4	0.68 V
Vref	1.17 V
C_{load}	> 5 μF
R_{esr}	> 0.5 Ω
Regulated output voltage	1.8 V
$I_{\text{load max.}}$	10 mA

The amplifier has a nMOS differential input stage, preferably for its higher mobility for achieving more gain. Reference voltage, V_{ref} will be bandgap voltage, 1.17 V, of silicon and thus ICMR for EA lies almost at half the supply voltage. This amplifier drives a pMOS buffer which is used to supply sufficient current to drive the large pass transistor. Moreover, pMOS as a buffer passes 1 better which means it can turn off the pass device completely and hence LDO regulates better at low load or no load condition. However for heavier load/larger load current, this pMOS buffer is not able to pull down the gate of pass device sufficiently lower. This is overcome by making the pass device large enough to feed the required maximum load current.

The pass device is a pMOS transistor in this design. It is chosen because it has several advantages over its counterparts like nMOS and BJT devices in terms of dropout voltage, quiescent current, input voltage, thermal response and noise[12]. Prominently, there are two factors that give pMOS edge over other devices; dropout voltage and quiescent current, when it comes to application in low power and low voltage devices. nMOS as a pass device requires a positive drive voltage with respect to output to operate. On the other hand, pMOS is driven by a negative signal with respect to input which means pMOS is

preferable for a low input LDO. Similarly compared to BJTs, pMOS requires less headroom and less quiescent current to be driven[12], [13], which means low dropout and low power operation, typical requirement of today's micro devices' power supply.

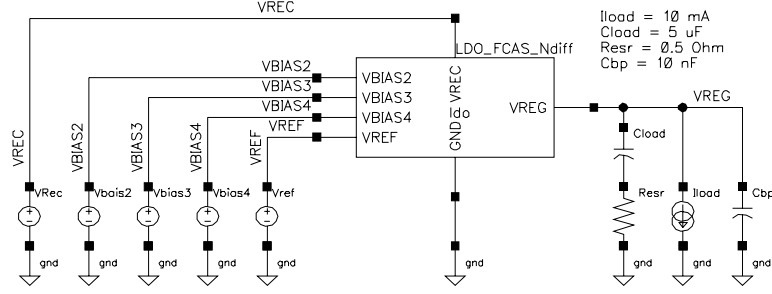


Figure 12: LDO testbench setup

However, pMOS as a pass device in LDO causes challenges in stability. As mentioned above, LDO utilises a high gain feedback loop in order to provide a regulated output voltages independent of load current and in any system with feedback loop, the locations of poles and zeros determine stability of the system. In case of the pMOS LDO, the pass device is configured in a common source configuration. LDO with big output cap has a dominant pole pole at the output, which is a low frequency pole. The second pole is located at the gate of pass device because as mentioned earlier pMOS pass device is large and has a big parasitic capacitance. This second pole may be located closer to the dominant pole, resulting in significant reduction in phase margin (PM). Consequently, this may lead to instability of the LDO with pMOS pass device. Various methods have been implemented for ensuring the stability of the pMOS LDO. In this project, a large external capacitor, C_{load} in figure 10, is used for stabilising the system at the cost of additional settling time. When an external capacitor is used for designing a stable LDO, the minimum value of capacitance, C_{load} and minimum value of its equivalent series resistance (ESR), R_{esr} should be specified[13]. C_{load} determines the dominant pole of the LDO and R_{esr} in series with C_{load} introduces a left half plane zero below unity gain frequency, UGF of LDO in order to cancel out the non-dominant pole below UGF, producing a stable LDO system.

3.2 Transient response

Figure 13 is the transient simulations of the LDO which illustrates generation of regulated output voltage, V_{reg} for both maximum load, 10 mA. For maximum load, it takes minimum 107 us to produce stable voltage. Since a large capacitor is used for stabilising LDO, it take longer time. Compared to schematic result, it takes 9 us extra time which can be accounted additional parasitic capacitance of interconnects at the output of LDO.

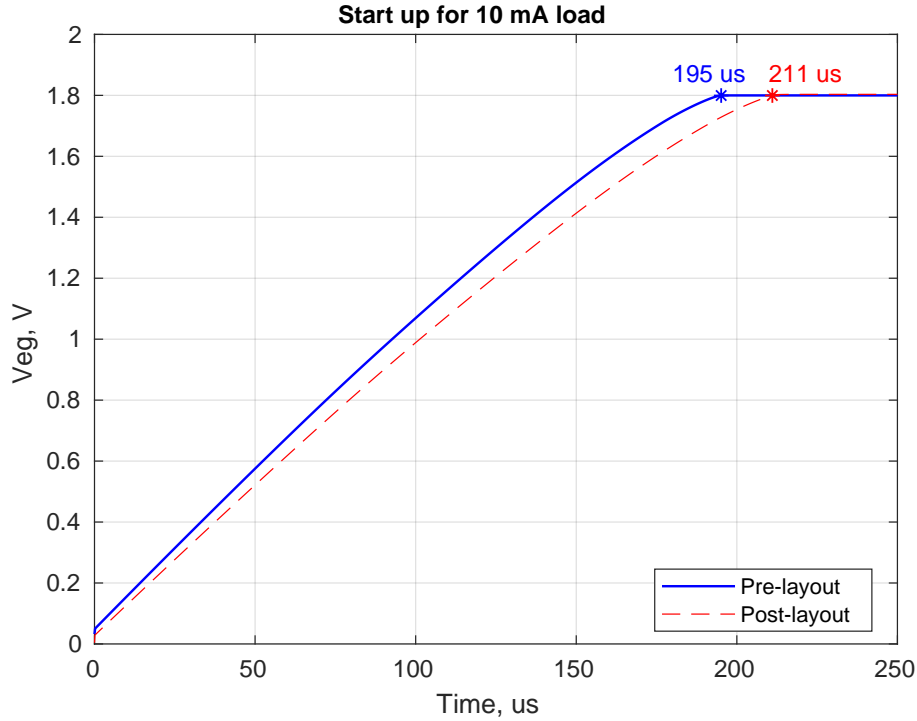


Figure 13: LDO transient simulation

Figure 14 and 15 show the transient response of LDO for line, V_{rec} and load, I_{load} variation. It gives information about how well and how fast regulated output settles for line and load variations. In figure 14 load is given as pulse varying from 10 uA to 10 mA with both falling and rising time of 1 ns keeping input supply constant to 2.2 V. Sudden increase in load causes the output voltage to drop. The error amplifier then takes some time adjusts the gate voltage of pass device to low to fully turn on the device. Likewise when the load suddenly drops to min-

imum, it causes the output voltage to increase. Again error amplifier adjust it back by increasing the gate voltage of pass device to turn it off. Similarly for line variation observation, input, V_{rec} is pulsed from 2 V to 2.5 V with 1 ns rising and falling time keeping load current constant to 10 mA. Sudden increase in input voltage causes output to increase and vice-versa. As in load variation case, similar recovery pattern is seen. In both case of load and line regulation, the out put voltage is maintained quickly, less than 0.15 us. Both results from schematic and post layout have same transition behaviour except post layout result offset by 3.7 mV as explained in DC response section below.

Line regulation, change in regulated output voltage due to maximum change in input voltage and load regulation, change in output voltage due to maximum change in load current are calculated from values shown in respective plots and are listed in table 5.

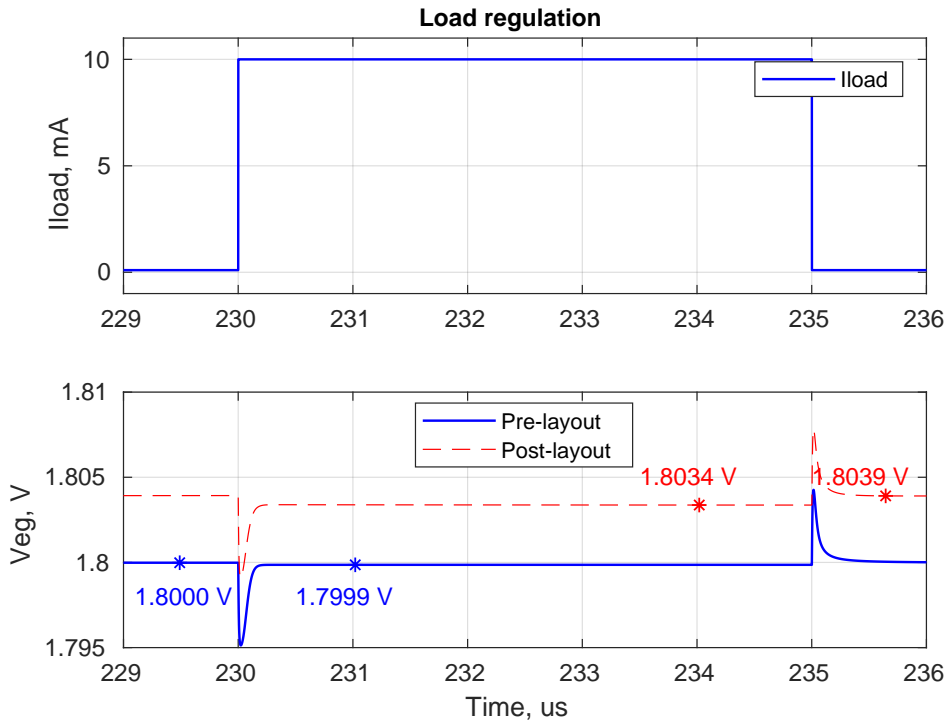


Figure 14: LDO step load regulation

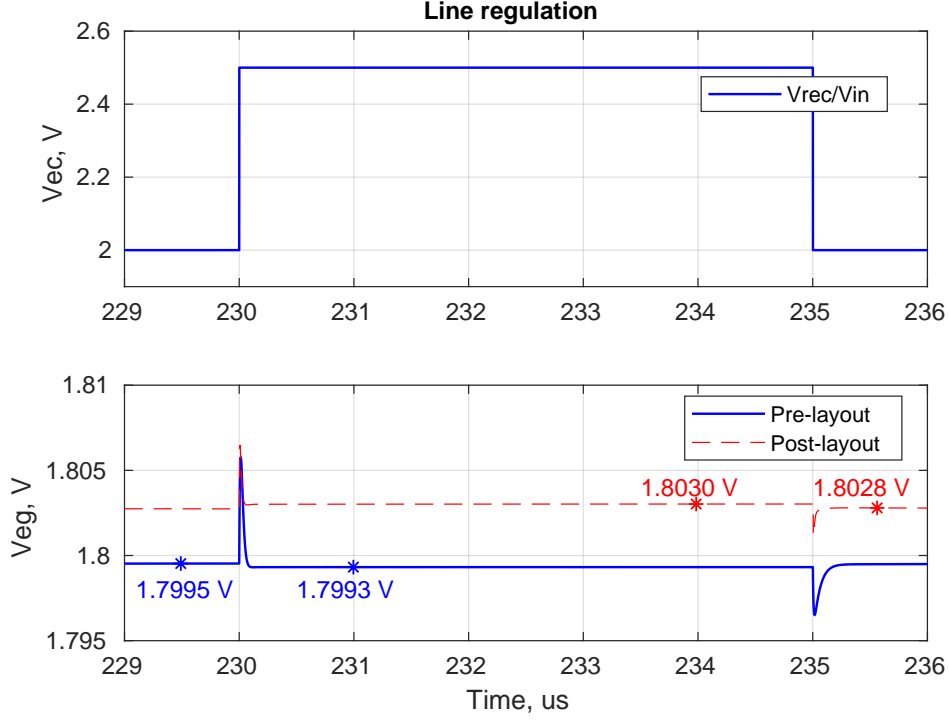


Figure 15: LDO step line regulation

3.3 DC response

Figure 16 and 17 show LDO response to input voltage, V_{rec} sweep and output load, I_{load} sweep. As seen in 16, the regulator is turned off for input below 1.85 V. Since the input is also the supply for the entire design, higher voltage is required for creating proper biasing of internal folded cascode error amplifier. However after turning on, it requires only 100 mV drop for proper regulation for maximum load and is even lesser for lighter load. This shows that minimum value of supply required for LDO to function properly is 1.95 V. In 17, it is seen that regulated output voltage for post layout simulation is 3.7 mV higher than for schematic. Since $V_{reg} = (1 + R1/R2) * V_{ref}$, the mismatch in the resistors has resulted in slightly higher ratio, consequently increasing the close loop gain.

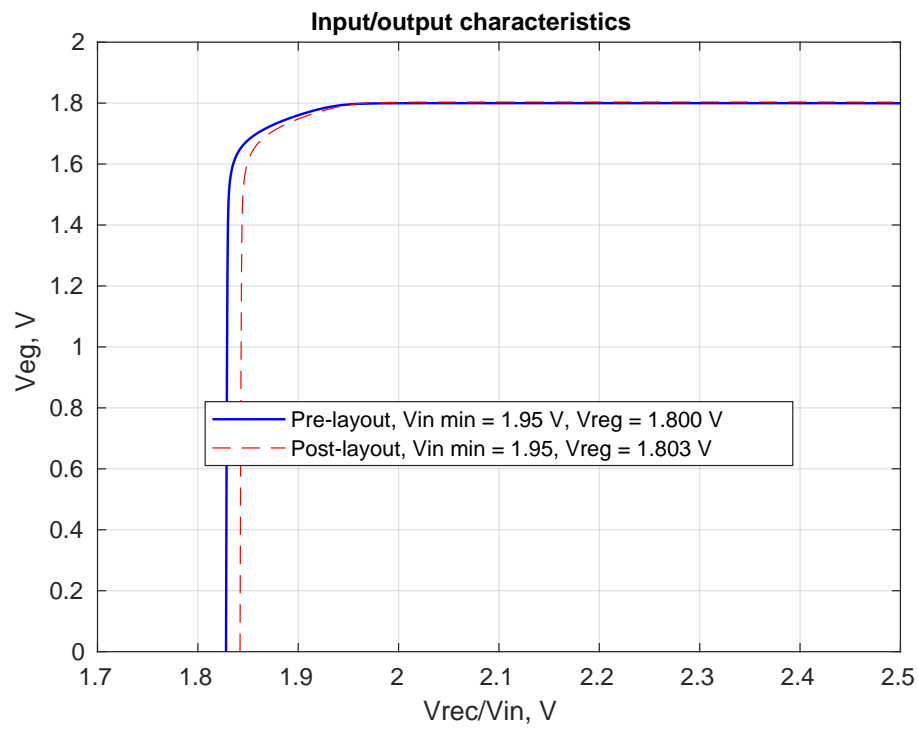


Figure 16: Regulated voltage with supply variation

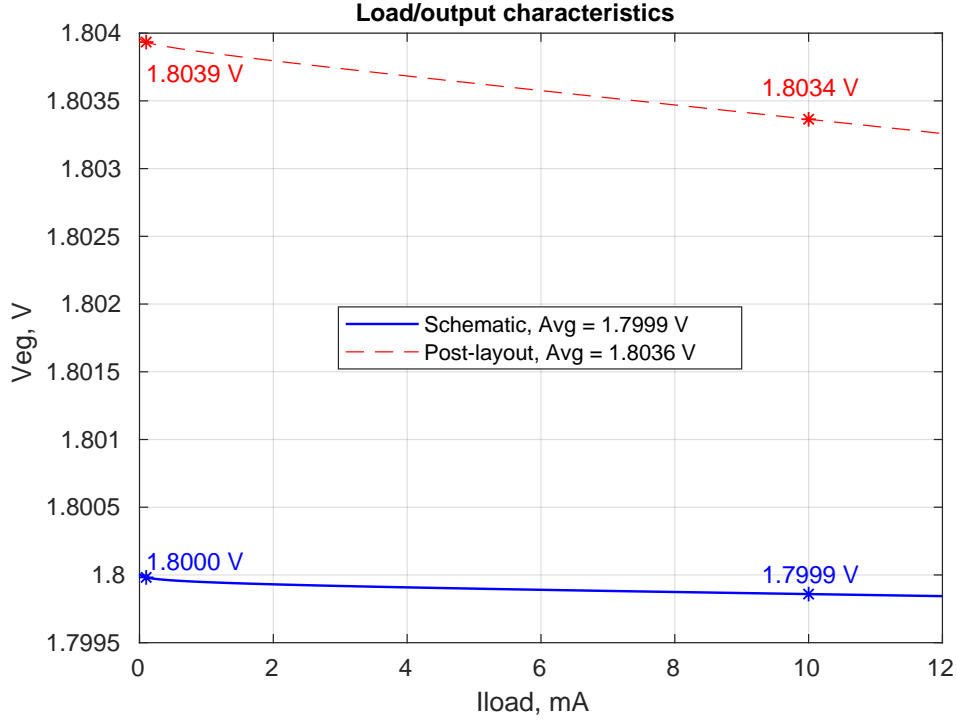


Figure 17: Regulated voltage with load variation

3.4 AC response

Figure 18 is open loop gain and phase margin of LDO without and with compensation. In the upper uncompensated bode plot, two poles below UGF are seen: the first one at 300 KHz due to output resistance of pass device and its parasitic capacitance, and the second one at 60 MHz due to buffer output resistance and gate capacitance of pass device. UGF is at 100 MHz. Due to these two poles both occurring below UGF, the PM fallen to -45° . For making the LDO stable, as discussed in the beginning, a capacitor, C_{load} , 2.5 μF with specific series equivalent resistance, R_{esr} , 0.8 Ω is used at the output. C_{load} and pass device output resistance creates the dominant pole at 1 KHz and R_{esr} and C_{load} creates a left half plane zero below UGF which cancels the non dominant pole. This eventually gives 75°PM and 30 dB GM.

Likewise figure 19 is the plot showing PSSR of this LDO. It can be seen that it has poor PSSR performance for frequency higher than 200 KHz. Low frequency noise like 50Hz supply ripple is effectively rejec-

ted. In this design 13.56 MHz ripple and its first harmonics is expected in the input of LDO because rectified output from rectifier operating at 13.56 MHz as input signal is used as supply and/or input for this LDO. Unfortunately, PSSR performance is worst around this frequencies. However the ripple rejection is still -36 dB at 13.56 MHz which is decent. As seen in figure 18, the open loop gain of LDO feedback circuit is 90 dB, which has contributed in achieving decent PSSR even at higher frequency[14]. This paper also discusses that UGF frequency corresponds to the roll off frequency of PSSR, which can also be seen by comparing plots 18 and 19. The stability technique in this design also gives adverse effect on PSSR performance as UGF is significantly lowered by large output capacitor.

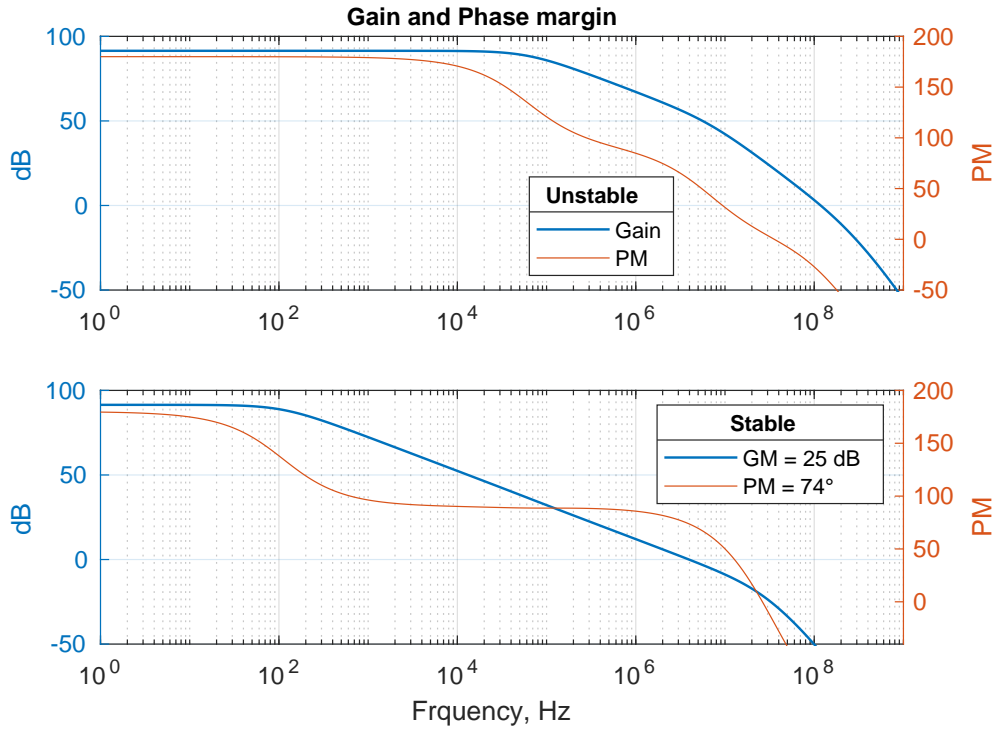


Figure 18: LDO stability before and after compensation

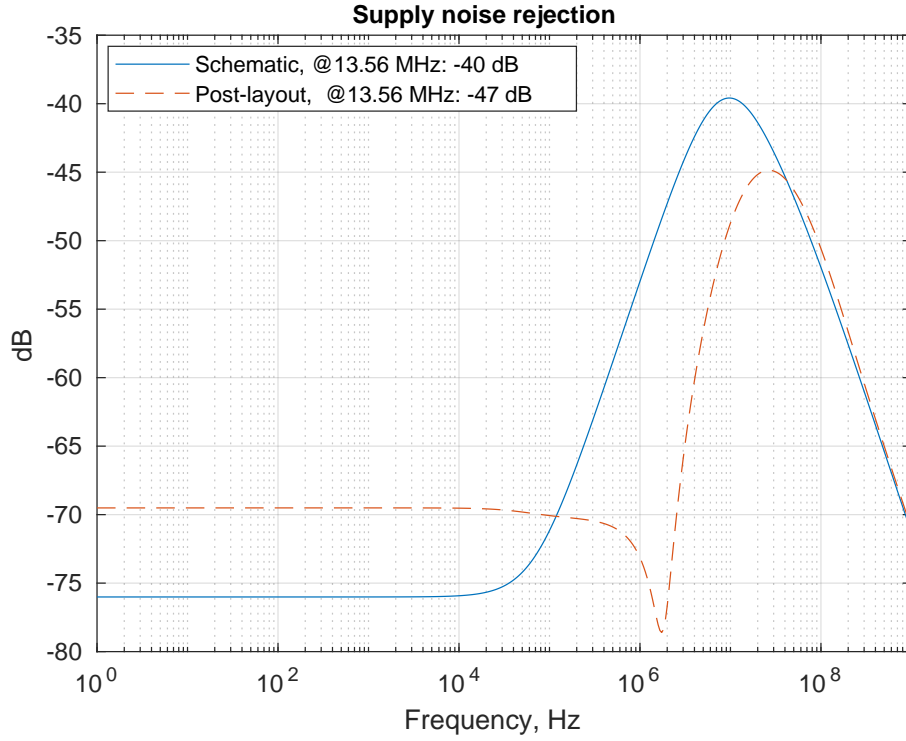


Figure 19: PSSR performance

Table 5 summaries the performance of LDO regulator discussed above. Power efficiency is calculated as power delivered to load to power consumed from the source. Quiescent current includes biasing currents for error amplifier, feedback resistors and buffer which is obtained by taking the difference of current drawn from the source and current delivered to the load. Both power efficiency and quiescent current is calculated for maximum load operation.

Table 5: LDO performance summary

	Schematic	Post-layout
PSSR	-40 dB @ 13.56 MHz	-47 dB @ 13.56 MH
Phase margin	75°	
Gain margin	30 dB	
Power efficiency	80.9 %	81 %
Quiescent current	105 uA	114 uA
Load regulation	13 uV/mA	54 uV/mA
Line regulation	395 uV/V	-511 uV/V

Reference and biasing circuit design follows next.

4 Reference and biasing

Reference and biasing circuit is important part of any analog circuit. It is required to bias the designed circuitry with proper voltages and currents for operating all the devices in the intended region. For reliable and consistent performance of the system, the references and biases should be independent of supply voltage and temperature variations. Moreover with the trend of shrinking device sizes, mismatch and process parameters variations have been so pronounced that these factors affect the operation of the devices. So for the today's devices, it is necessary to design reference and biasing independent of PVT variations.

There are different methods of generating reference voltages and bias currents discussed in literatures. Basically, supply independent current source is generated first and then this current is passed through a resistor to get a reference voltages. Some ways of creating supply insensitive current sources are threshold voltage referenced, diode (V_{BE} in BJT) referenced thermal voltage referenced current sources [15, pp. 305-315]. However, these current sources are not temperature independent. Threshold voltage of MOS and forward voltage of diode or V_{BE} have a negative temperature coefficient TC and hence they produce a CTAT (complementary to absolute temperature) current. On the other hand, the thermal voltage (V_T) has positive TC and hence it produce a PTAT (proportional to absolute temperature) current. So these techniques, though being insensitive to supply variations, still cannot be used for accurate reference voltage generation because of temperature dependence. So bandgap reference (BGR) design is used to generate the required reference voltage for the LDO in this design which has significantly less PVT variations than the last three methods.

BGR design involves summing up two voltages of which one is PTAT and the other is CTAT, both having equal and opposite TCs. The equal and opposite TCs cancels out leaving the resultant voltage with a zero TC. Figure 20 is the CMOS implementation of reference and biasing circuit for this project which includes startup circuit, BGR circuit and biasing circuit.

PTAT current is first generated using thermal voltage referenced current source using PNP transistor as diodes, resistor and a op-amp controlled current mirror [11, pp. 391-392]. The current is $I = V_T \ln(n)/R_1$, where $V_T = kT/q$ is thermal voltage with positive TC and n is number

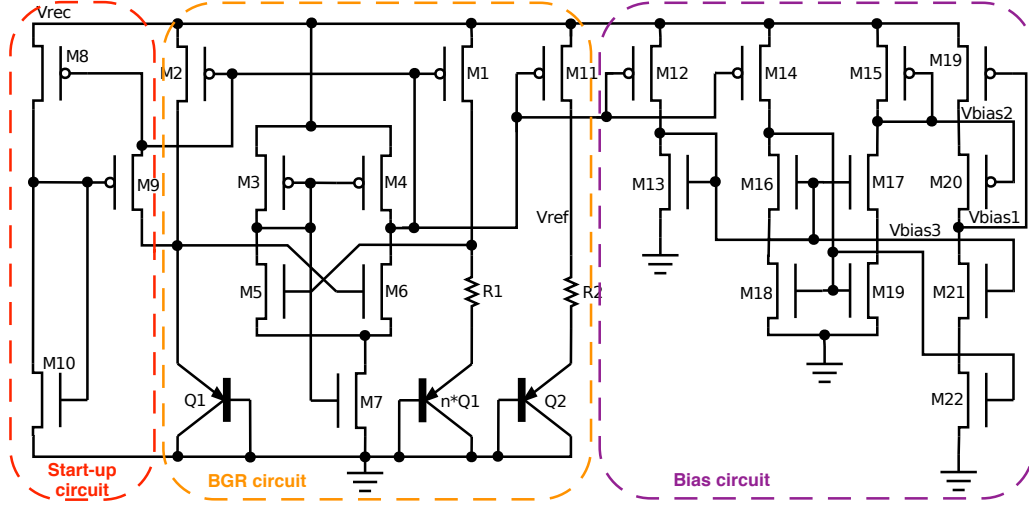


Figure 20: BGR and bias generation circuit

of parallel PNP transistors. This current is passed through a resistor, R_2 to create a PTAT voltage which is in series with a diode realised with a parasitic PNP transistor. The value of R_2 is so chosen such that the positive TC of PTAT voltage across it is equal to negative TC of V_{BE} . The temperature independent reference voltage is then given as $V_{ref} = V_{BE} + \alpha V_T \ln(n)$, where $\alpha = R_2/R_1$ is equal to $\Delta V_{BE}/\Delta T$. Similarly the folded cascode operational transconductance amplifier (OTA) working as an error amplifier in LDO requires additional bias voltages which are produced as shown. Wide swing current mirror topology is used here for bias voltage generation.

In case of the supply independent and self biased circuit, there may be start-up issue. If all the transistors carry zero current, they may indefinitely remain off even when the supply is turned on. Therefore start-up circuit is added in order to ensure that the devices are turn on as supply voltage is provided. Once the circuit is fully operational, the start-up circuit is off and does not effect the normal operation of BGR circuit.

Figure 21, 22 and 23 illustrates temperature, DC and transient simulation of the BGR circuit respectively for slow(ss), fast(ff) and typical(tt) corners. The plots shows that V_{ref} is fairly independent with PVT variations. Similarly, I_{bias} variations used for generating the bias voltages remains within considerable range. Table 6 summarises the

performances of the BGR design.

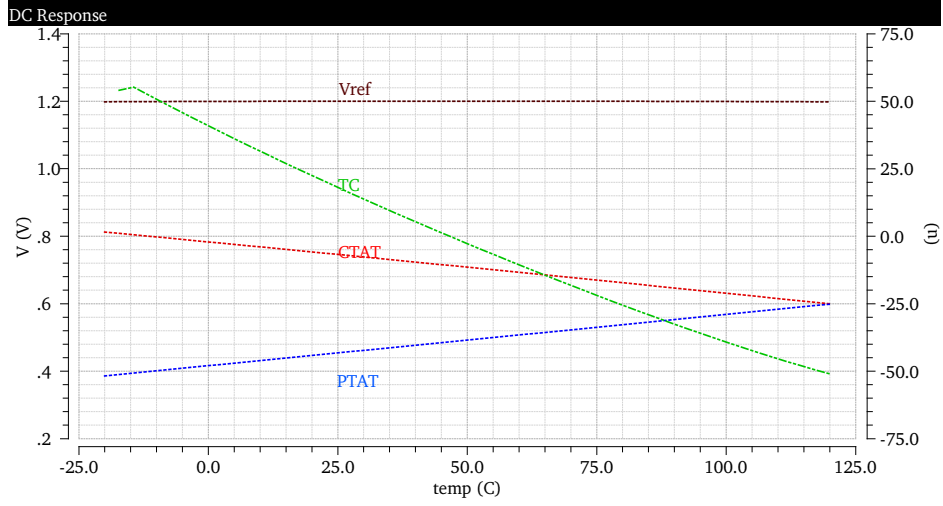


Figure 21: BGR over temperature variation

Table 6: BGR parameter and performance

V_{ref}	1.201.1 V @slow corner
	1.201.4 V @fast corner
	1.200.1 V @typical corner
TC @27°C	16.4 $\mu\text{V}/^\circ\text{C}$
I_{bias}	8.95 μA @slow corner
	11.37 μA @fast corner
	10.04 μA @typical corner

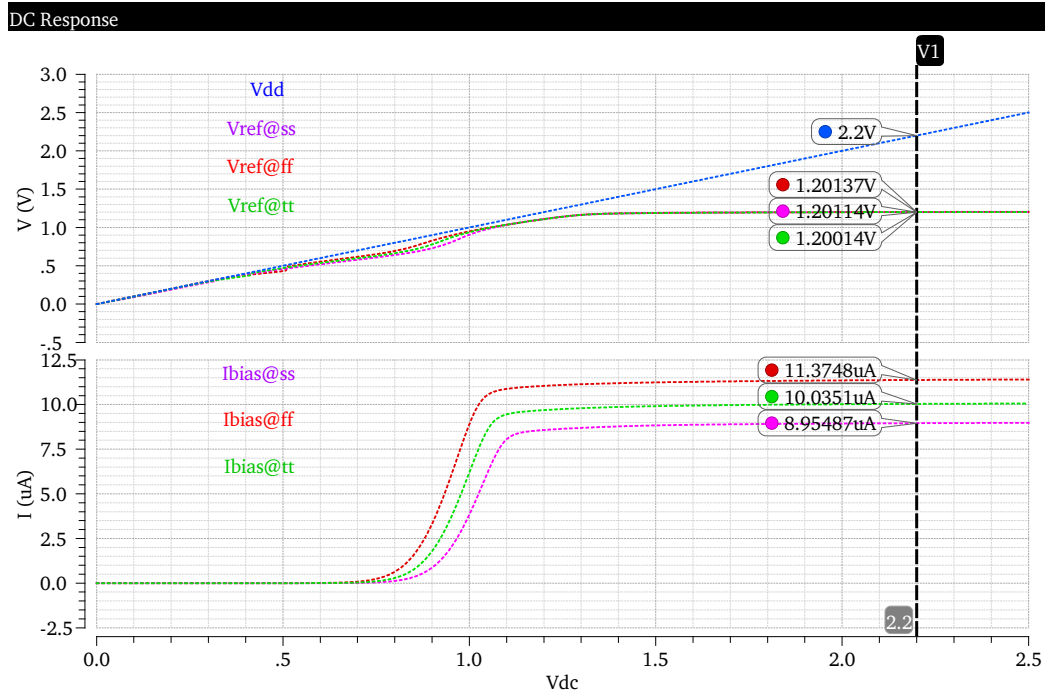


Figure 22: BGR DC performance

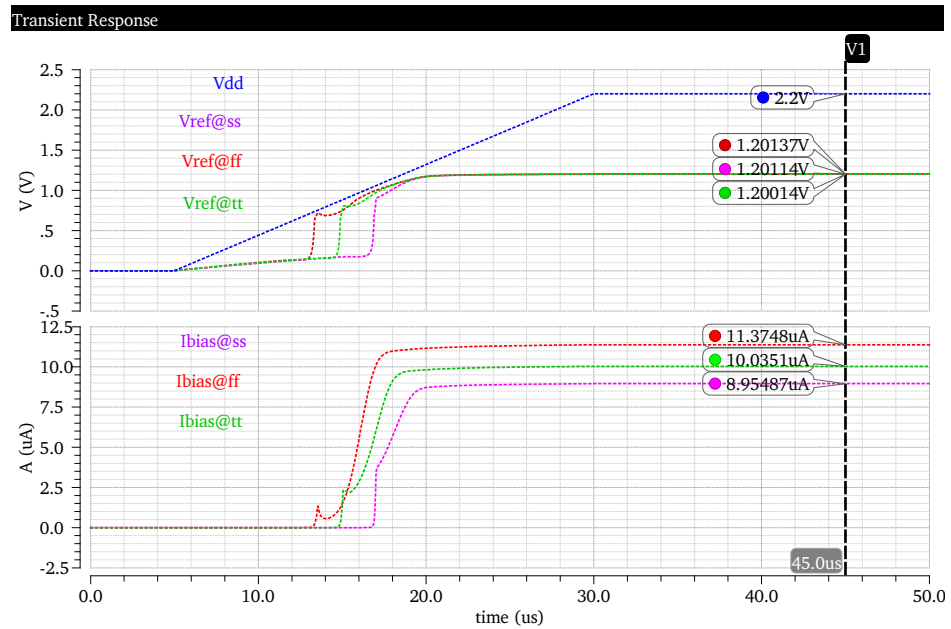


Figure 23: BGR transient performance

5 Antenna Design

All the components discussed above are part of any power management system which takes DC input from power line and creates regulated output as required. However, the objective here is to replace direct power line connection with wireless link. Since the intention is to just create a wireless power transfer link, the option which is easier to implement, convenient to operate and gives higher transfer efficiency is the primary choice here. And the literatures in wireless power transfer studies show inductive coupling meets all these requirement.

Inductive coupling boils down to principle of electromagnetic induction. When alternating electric current is passed through a coil, say primary, it generates alternating magnetic field. If another coil, say secondary, is placed in this changing magnetic field, alternating voltage/current is induced in the coil. In other word, power from primary coil is transferred wirelessly to secondary coil through magnetic field and this is popularly known as inductive power transfer link. And this induced ac voltage is rectified and then used to power up the load.

The energy transfer efficiency between the coils depends on how much of the magnetic field generated by the primary is captured by the secondary coil. And the capture of magnetic field by the secondary coil in turn depends on shape and size of two coils, their separation and alignment. All these factors influencing the transfer efficiency collectively gives a quantity called coupling factor, k . A perfect inductive link has a coupling factor 1, which means all the magnetic flux generated by primary is captured by secondary. However normally achieved coupling factor in practical inductive link is 0.3 and at best 0.5. So for better transfer of efficiency, some improvisation is done to the inductive link, so that efficiency is less affected by coil separation and alignment. This is done by tuning both the primary and secondary coil to same frequency i.e. creating resonance at some frequency so that coil coupling is the strongest at that frequency. This method of creating better wireless energy transfer link is popularly known as magnetic resonance coupling.

In this project, first an antenna coil is designed and characterised. Then inductive link created using that antenna is studied and finally magnetic resonance technique is implemented to increase transfer efficiency at the operating frequency. The antenna dimensions are provided

by Nordic Semiconductor which is one of their design already used in some application. Since having similar shape and size of antennas is important in gaining more transfer efficiency, the same antenna type is used as both primary and secondary coils.

5.1 Inductor model

Figure 24 is a lumped model of a planar antenna/coil/inductor made on a PCB. R_p , series DC resistance of wire and C_p , inter-winding self capacitance. These parasitics determine quality factor and self resonance frequency, SRF of the antenna. The quality factor is given as $Q = \omega L / R_p$ and SRF as $SRF = 1/(\sqrt{LC_p})$, for this simple model.

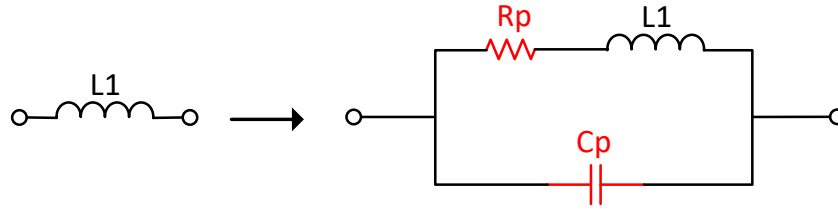


Figure 24: Real antenna model

For purpose of this work, with provided dimensions of the antenna, it is first modelled in HFSS as shown in figure 25a and its equivalent lumped circuit in figure 25b. It is important to note here that L1 in 25b is in fact 24. However, in the discussion ahead, these parasitics are not explicitly mentioned for simplicity because the parameter extraction will include these factors too and on the other hand the operating frequency here is much less than coil SRF. To realise a real antenna, physical parameters of materials used for making printed antenna on a PCB are also given for the model. After completing model, frequency sweep is done for extracting S parameter of the antenna which was eventually used to estimate self inductance of the modelled coil. The performance estimation of single antenna here and couple system later is based on formulas in [16]. In order to check and compare the estimated inductance value from the model, Modified Wheeler Formula, a mathematical approximation model described in [17] is used. The qualities of antenna obtained from extracted S-parameter are listed in

table 7. The table shows that modelled inductance value is less than mathematically approximated value. This difference can be explained with two things. Firstly, mathematical calculation assumed that the antenna is spiral and rectangular with sharp edge but the model has rounded edge. Secondly, during modelling besides dimensions of the coils, physical parameters of coil materials are also used but these are not considered for mathematical calculation.

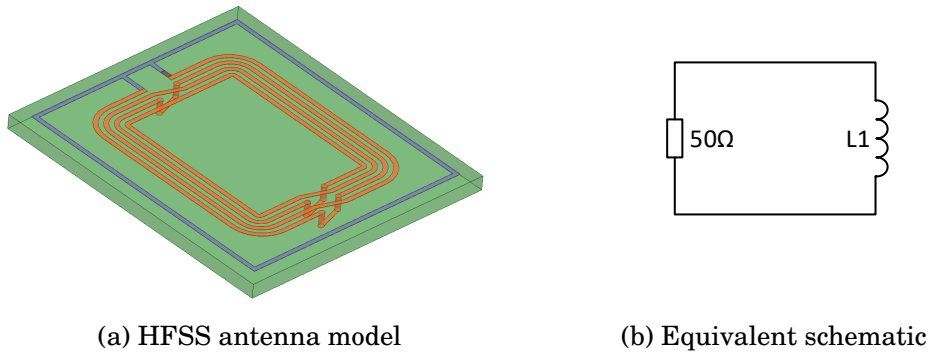


Figure 25: Antenna model

Table 7: Characterisation of antenna

	HFSS model	Modified Wheeler [17]
Self Inductance	448 nH	644 nH
SRF	125 MHz	
Quality factor		
Parasitic Resistance		
Parasitic Capacitance		

5.2 Inductive link: coupled coils

In the next step, an inductive link is realised by using two antennas: one as primary and other as secondary, aligned one over other and separated by air gap as shown in figure 26a, equivalently shown as lumped

schematic in figure 26b. Coupling system of these antennas is simulated for varying distance of magnetic field interaction to observe the difference in performance. The same procedure as used for single coil above, is used to extract self inductance of each coil, $L1$ and $L2$, mutual inductance of two coils, $L12$, coupling coefficient between the coils, k and quality factor, Q . The extracted values for coil separation of 1mm, 5mm and 10mm are listed in table 8 calculated at operating frequency of 13.56 MHz.

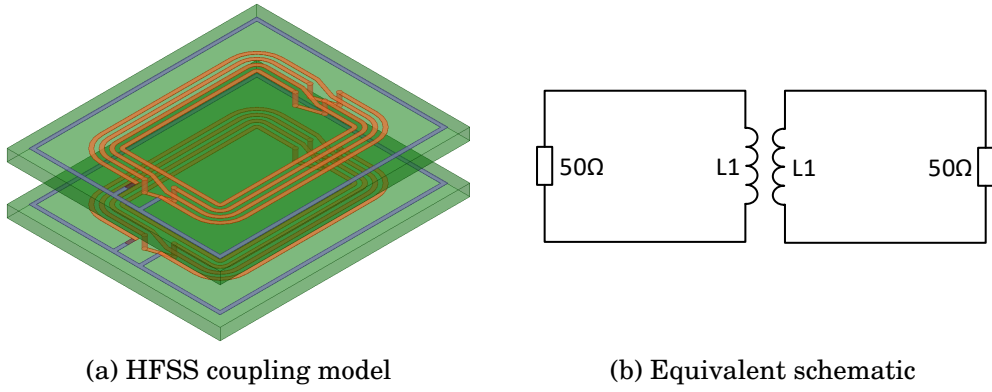


Figure 26: Antenna coupling model

Table 8: Coupling parameters for varying coils distance

Parameter	1 mm	5 mm	10 mm	mm
L1	-	-	-	nH
L2	-	-	-	nH
L12	-	-	-	nH
k	-	-	-	-
Q	-	-	-	-
SRF				

It is observed that $L1$ and $L2$ are same as in table 7 as it is the same coil used as primary and secondary. Similarly $L12$ and k , related as $L12 = k\sqrt{(L1L2)}$, are both decreasing with distance as expected. With increase in separation, less and less magnetic flux generated by

primary coil is linked with the secondary, creating a loosely coupled inductive link.

The power transfer efficiency of the physical link created by coupled coils is very important. [CITE] states that efficiency depends k of coupling system and Q of coil and hence high k and high Q is always desirable and obviously coil optimisation is the most important part of coupling system design. [18] and [19] discusses some techniques to optimise transfer efficiency of inductive link: [18] about matching the load for better resonance whereas [19] about designing optimal coil geometry for higher Q . The former one compares the efficiency of general inductive coupling and conventional resonant coupling and their limitation in achieving higher efficiency. This eventually proposes optimal resonant load transformation which has better immunity to poor coupling and load variation. Likewise, the later one describes step by step iterative process of designing an antenna with optimal geometry for the given design constraints.

5.3 Magnetic Resonance Coupling

In this project, conventional magnetic resonance coupling as in is implemented to tune both primary and secondary to the power carrier frequency. The purpose here is to match the impedance of primary antenna to source impedance and secondary antenna of coupling system to load impedance in order to maximise the power transmission from the source to the load.

For the purpose of making a resonant inductive link, the S parameter of coupled antenna system in HFSS is exported to ADS in order to design matching networks using capacitors only. Impedance of primary antenna is matched to $50\ \Omega$ source resistance and impedance of secondary is matched to load impedance ($50\ \Omega$ load or input impedance chip(?)) as shown in 27. C_{p1} , series capacitor and C_{p2} , shunt capacitor together with $L1$ created parallel resonant circuit at 13.56 MHz on the primary side and C_{s1} , shunt capacitor together with $L2$ creates the secondary resonant circuit at same operating frequency. Thus a pair of LC tank circuit is made tuned at same frequency. Such matching network is designed for all three coil separation distances as above, but resonant coupling system with 5 mm separation is taken as a typical example and presented here.

The reflection power loss, S11 and S22, at both primary and secondary terminal, power transfer gain, S21, from primary to secondary and Q-factors for both antennas before and after creating resonance are shown in figure 28, this and this.

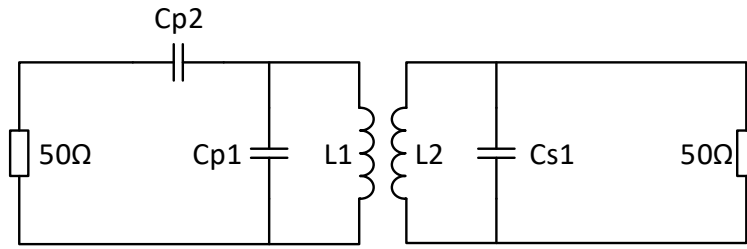


Figure 27: Resonant coupled inductive link

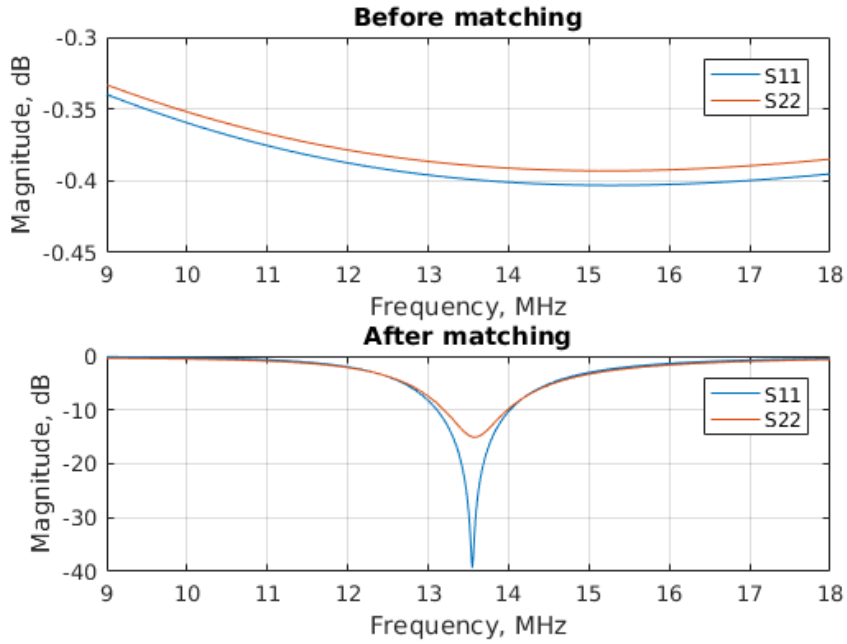


Figure 28: Power loss before and after matching

The performance of magnetic resonant coupling link designed in this work is summarises in table 9 below.

Table 9: Performance of resonant inductive link

C_{p1} C_{p2} and C_{s1}	
Resonant frequency	13.56
Primary reflection loss	
Secondary reflection loss	
Primary to secondary gaining	http://beta.goal.com/en/news/mbappe-born-to-be-the-best
Q-factor	

6 Power Receiving Unit

Wireless power transfer, WPT system always constitutes two main units: power transmitting unit, PTU and power receiving unit, PRU. Each unit comprises of resonator, power conditioner and control circuits as shown in figure 29. Both the resonators in PRU and PTU are tuned to operating frequency, which create a physical transfer link. Power conditioner circuit in PTU includes at least power amplifier and matching circuit, whereas in PRU, it includes matching circuit, rectifier and regulator. Similarly both these units have control block which facilitates transfer procedure and communication between these units. In this work, design and analysis of PRU is the main objective.

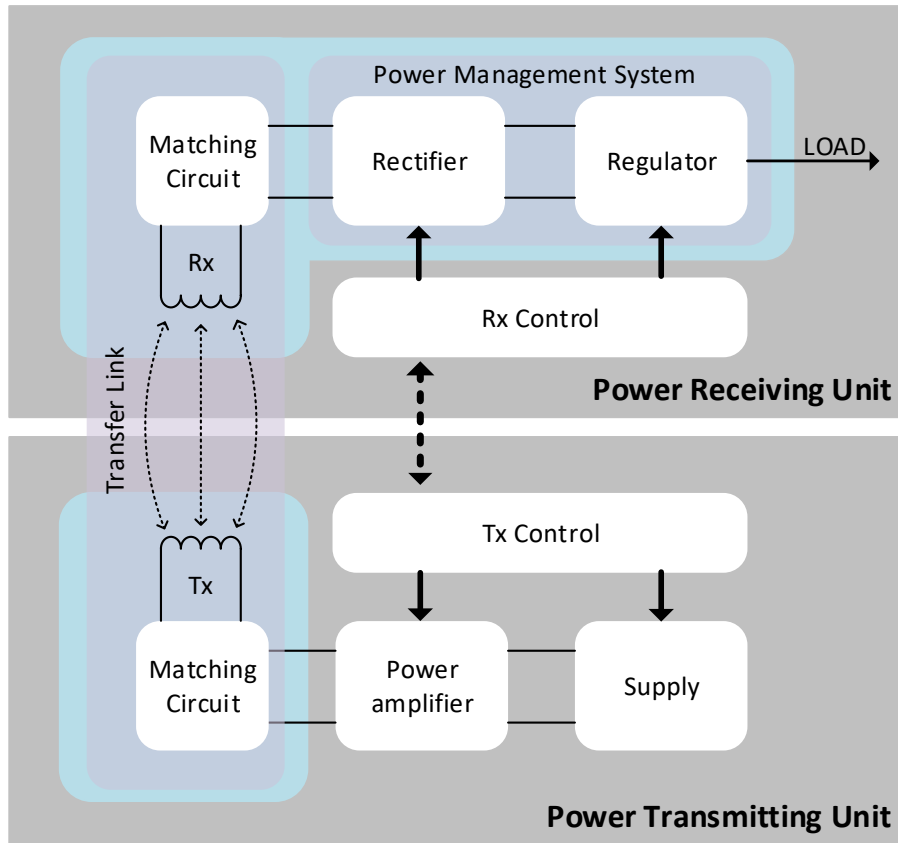


Figure 29: WPT block diagram

In figure 29 above, the block highlighted in blue is the PRU system in this design. Secondary coil, Rx is the receiver resonator, and

rectifier and regulator is power conditioning block. The primary coil is driven by a power source and AC signal is generated at the secondary as discussed earlier in antenna design section. The rectifier then rectifies this AC signal to DC. The DC output of the rectifier is then fed to LDO to produce regulated DC output required to drive a load. The reference and biasing circuit generates required reference and biasing DC voltages for the LDO.

The PRU unit is broken down into two sub units for step wise analysis. As seen in the block diagram, it is functionally divided into Transfer Link and Power Management System (PMS). Firstly, PMS is simulated excluding the transfer link to characterise the performance of PMS. Secondly, the whole PRU system: PMS with transfer link created with coupled antenna, Tx and Rx, is simulated to observe the performance of whole PRU. Though it has already been told earlier, one important thing must be mentioned here again before going further. Even though reference and biasing circuit has been integrated into the PMS system, it has been designed with an option to override it externally. This externally supplied reference and biasing will be primarily used for the PRU system simulation. The result with on-system biases and reference will be explicitly noted when used.

7 Power Management System

Figure 30 is the top level of PMS in this design and test bench setup is shown in figure 31. The purpose here is to give differential signal Vin1 and Vin2 from source Vac and see Vrec and Vreg outputs while driving maximum load. The other inputs are external biases, reference, control and supply for LDO and buffer. Other outputs are biases voltages to examine the performance of BGR circuit which is disabled now with external control signal Vctl low.

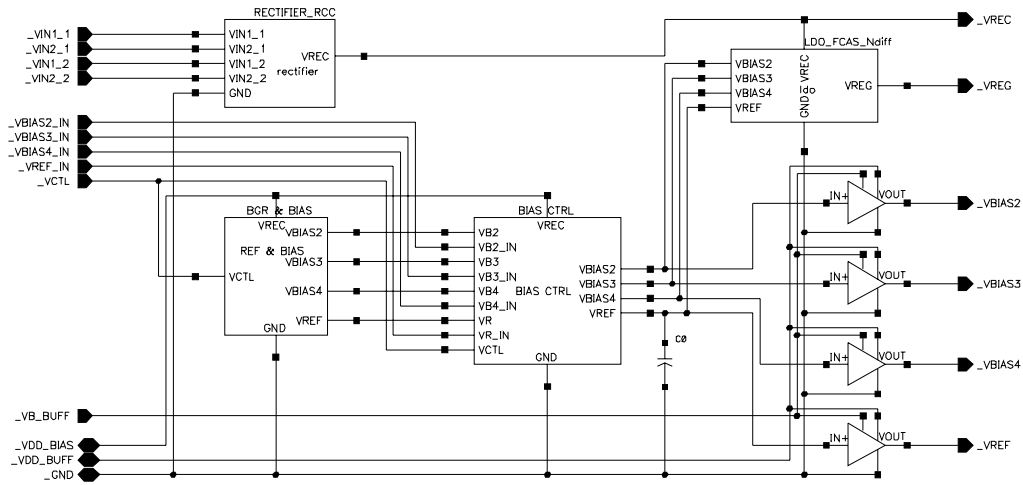


Figure 30: WPT PMS implementation

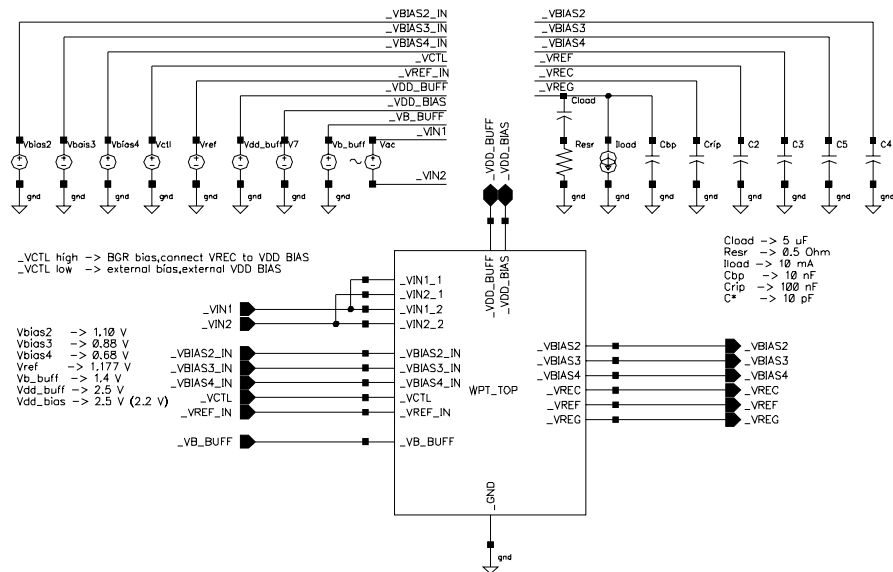


Figure 31: Test bench for PMS simulation

8 Transient Response

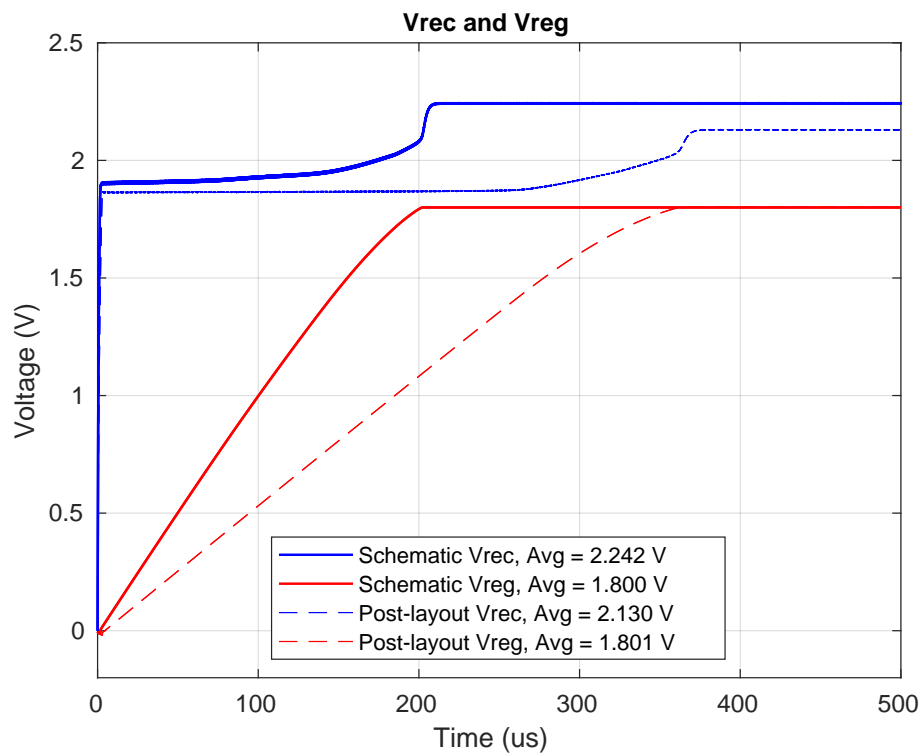


Figure 32: Transient

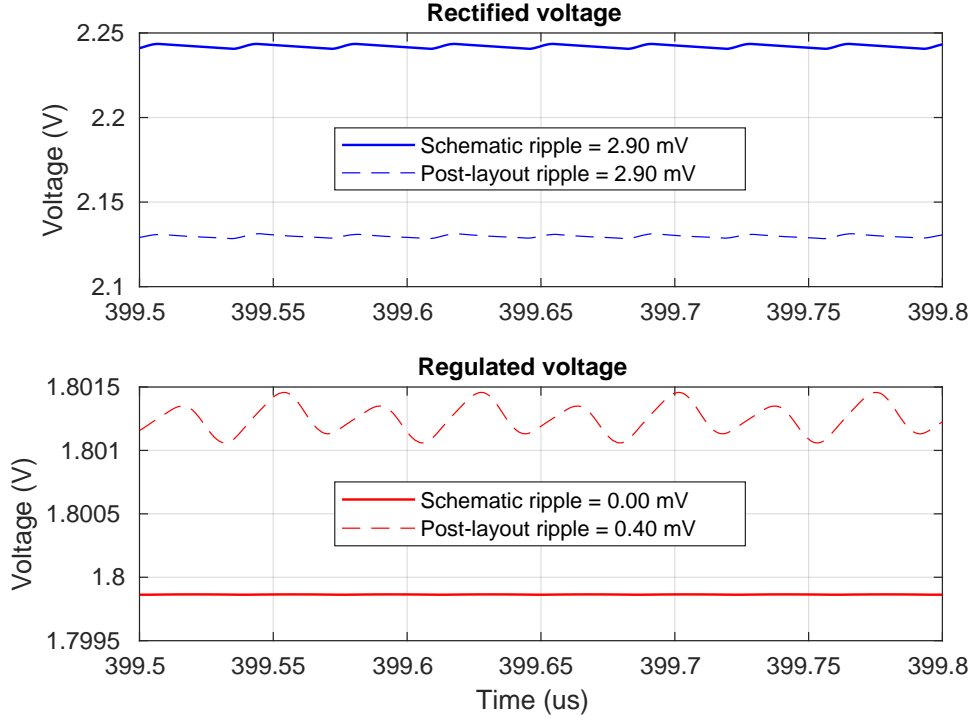


Figure 33: Ripple in V_{rec} and V_{reg}

9 PRU Unit

Figure 34 is test bench for complete PRU unit. It includes PMS shown in figure 30 and resonant inductive link shown in figure 26. This inductive link is coupling model extracted from HFSS and both antennas tuned at the operating frequency, 13.56 MHz. The primary antenna is driven by signal source V_{ac} and the secondary antenna generate differential signal V_{in1} and V_{in2} , the inputs for the chip. Other biasing voltages and component values remain the same as in PMS simulation.

SMA connectors are used. Similarly, for decoupling and ripple rejection SMD MLCC capacitors are used but for stability purpose of LDO, electrolytic capacitor is used owing to requirement of better accuracy and higher ESR for compensation capacitor. In order to have better control of supplies to bias, buffer and pad circuits on board regulator is used. For convenience, instead of providing biases voltages from power supply, on board resistive network is implemented to generate required bias voltages. For sanity check of the chip, balun is used to create differential signal inputs. The test PCB and antenna are shown in figure [figure].

References

- [1] Lopez Research. *An Introduction to the Internet of Things (IOT)*. Retrived from: http://www.cisco.com/c/dam/en_us/solutions/trends/iot/introduction_to_IoT_november.pdf. Nov. 2013.
- [2] Jan Rabaey. *Low Power Design Essentials*. 1st. Springer Publishing Company, Incorporated, 2009. ISBN: 0387717129, 9780387717128. DOI: [10.1007/978-0-387-71713-5](https://doi.org/10.1007/978-0-387-71713-5).
- [3] Loreto Mateu and Francesc Moll. 'Review of energy harvesting techniques and applications for Microelectronics'. In: *Proceedings of SPIE - The International Society for Optical Engineering*. Vol. 5837. June 2005.
- [4] S. S. Hashemi, M. Sawan and Y. Savaria. 'A High-Efficiency Low-Voltage CMOS Rectifier for Harvesting Energy in Implantable Devices'. In: *IEEE Transactions on Biomedical Circuits and Systems* 6.4 (Aug. 2012), pp. 326–335. ISSN: 1932-4545. DOI: [10.1109/TBCAS.2011.2177267](https://doi.org/10.1109/TBCAS.2011.2177267).
- [5] Y. H. Lam, W. H. Ki and C. Y. Tsui. 'Integrated Low-Loss CMOS Active Rectifier for Wirelessly Powered Devices'. In: *IEEE Transactions on Circuits and Systems II: Express Briefs* 53.12 (Dec. 2006), pp. 1378–1382. ISSN: 1549-7747. DOI: [10.1109/TCSII.2006.885400](https://doi.org/10.1109/TCSII.2006.885400).
- [6] H. M. Lee and M. Ghovanloo. 'An Integrated Power-Efficient Active Rectifier With Offset-Controlled High Speed Comparators for Inductively Powered Applications'. In: *IEEE Transactions on Circuits and Systems I: Regular Papers* 58.8 (Aug. 2011), pp. 1749–1760. ISSN: 1549-8328. DOI: [10.1109/TCSI.2010.2103172](https://doi.org/10.1109/TCSI.2010.2103172).
- [7] Gaurav Bawa and Maysam Ghovanloo. 'Analysis, design, and implementation of a high-efficiency full-wave rectifier in standard CMOS technology'. In: *Analog Integrated Circuits and Signal Processing* 60.1 (2009), pp. 71–81. ISSN: 1573-1979. DOI: [10.1007/s10470-008-9204-7](https://doi.org/10.1007/s10470-008-9204-7).
- [8] Ian Poole. *PSU | Linear Power Supply*, *Radio-electronics.com*. Retrived from: <http://www.radio-electronics.com/info/power-management/linear-power-supply-psu/basics-tutorial.php>. Sept. 2012.

- [9] K. Keikhosravy and S. Mirabbasi. 'A 0.13-um CMOS Low-Power Capacitor-Less LDO Regulator Using Bulk-Modulation Technique'. In: *IEEE Transactions on Circuits and Systems I: Regular Papers* 61.11 (Nov. 2014), pp. 3105–3114. ISSN: 1549-8328. DOI: [10.1109/TCSI.2014.2334831](https://doi.org/10.1109/TCSI.2014.2334831).
- [10] G. A. Rincon-Mora and P. E. Allen. 'A low-voltage, low quiescent current, low drop-out regulator'. In: *IEEE Journal of Solid-State Circuits* 33.1 (Jan. 1998), pp. 36–44. ISSN: 0018-9200. DOI: [10.1109/4.654935](https://doi.org/10.1109/4.654935).
- [11] Behzad Razavi. *Design of Analog CMOS Integrated Circuits*. 1st ed. New York, NY, USA: McGraw-Hill, Inc., 2001. ISBN: 0072380322, 9780072380323.
- [12] Brian M. King. *Advantages of using PMOS-type low-dropout in-ear regulators in battery applications*. Retrived from: http://www.ti.com/sc/docs/apps/msp/journal/aug2000/aug_04.pdf. Aug. 2000.
- [13] Everett Rogers. *Stability analysis of low-dropout linear regulators with a PMOS pass element*. Retrived from: <http://www.ti.com/lit/an/slyt194/slyt194.pdf>. 1999.
- [14] John C. Teel. *Understanding power supply ripple rejection in linear regulators*. Retrived from: <http://www.ti.com/lit/an/slyt202/slyt202.pdf>. 2005.
- [15] Paul R. Gray et al. *Analysis and Design of Analog Integrated Circuits*. 5th. New York, NY, USA: Wiley Publishing, 2009. ISBN: 978-0-470-24599-6.
- [16] M. Drakaki, A. A. Hatzopoulos and S. Siskos. 'CMOS Inductor Performance Estimation using Z- and S-parameters'. In: *2007 IEEE International Symposium on Circuits and Systems*. May 2007, pp. 2256–2259. DOI: [10.1109/ISCAS.2007.378732](https://doi.org/10.1109/ISCAS.2007.378732).
- [17] S. S. Mohan et al. 'Simple accurate expressions for planar spiral inductances'. In: *IEEE Journal of Solid-State Circuits* 34.10 (Oct. 1999), pp. 1419–1424. ISSN: 0018-9200. DOI: [10.1109/4.792620](https://doi.org/10.1109/4.792620).
- [18] R. F. Xue, K. W. Cheng and M. Je. 'High-Efficiency Wireless Power Transfer for Biomedical Implants by Optimal Resonant Load Transformation'. In: *IEEE Transactions on Circuits and Systems I: Regular Papers* 60.4 (Apr. 2013), pp. 867–874. ISSN: 1549-8328. DOI: [10.1109/TCSI.2012.2209297](https://doi.org/10.1109/TCSI.2012.2209297).

- [19] U. M. Jow and M. Ghovanloo. ‘Design and Optimization of Printed Spiral Coils for Efficient Transcutaneous Inductive Power Transmission’. In: *IEEE Transactions on Biomedical Circuits and Systems* 1.3 (Sept. 2007), pp. 193–202. ISSN: 1932-4545. DOI: [10.1109/TBCAS.2007.913130](https://doi.org/10.1109/TBCAS.2007.913130).
- [20] R. Jacob Baker. *CMOS Circuit Design, Layout, and Simulation*. 3rd. Wiley-IEEE Press, 2010. ISBN: 0470881321, 9780470881323.
- [21] David A Johns and Ken Martin. *Analog integrated circuit design*. 2E. John Wiley & Sons, 2012. ISBN: 978-1-118-09233-0.

List of Figures

1	Block diagram of complete design	1
2	Rectifier topologies: conventional and gate cross coupled	8
3	Gate cross coupled full wave active rectifier]	9
4	Comparator circuit, RCC	10
5	Testbench for rectifier	12
6	Voltage and current waveforms of the rectifier	12
7	Voltages waveform for pre and post layout	13
8	Rectified DC output for pre and post layout	14
9	Voltage and power conversion efficiency	15
10	Generic LDO with pMOS pass device	17
11	CMOS implemenation of LDO	18
12	LDO testbench setup	20
13	LDO transient simulation	21
14	LDO step load regulation	22
15	LDO step line regulation	23
16	Regulated voltage with supply variation	24
17	Regulated voltage with load variation	25
18	LDO stability before and after compensation	26
19	PSSR performance	27
20	BGR and bias generation circuit	30
21	BGR over temperature varitaion	31
22	BGR DC performance	32
23	BGR transient performance	32
24	Real antenna model	34
25	Antenna model	35
26	Antenna coupling model	36
27	Resonant coupled inductive link	38
28	Power loss before and after matching	38
29	WPT block diagram	40
30	WPT PMS implementation	42
31	Test bench for PMS simulation	42
32	Transient	43
33	Ripple in Vrec and Vreg	44
34	Test bench for complete PRU unit	45

List of Tables

1	Project specifications	2
2	Rectifier design parameters	11
3	Rectifier performance summary	16
4	LDO design parameters	19
5	LDO performance summary	28
6	BGR parameter and performance	31
7	Characterisation of antenna	35
8	Coupling parameters for varying coils distance	36
9	Performance of resonant inductive link	39

Acronyms

BGR	bandgap reference
CMOS	complementary metal-oxide-semiconductor
CTAT	complementary to absolute temperature
DC	direct current
ESR	equivalent series resistance
GM	gain margin
ICMR	input common mode range
JLCC	J-Lead Chip Carrier
LDO	linear dropout
MLCC	Multi-Layer Ceramic Capacitor
MOS	metal-oxide-semiconductor
nMOS	n-channel MOS
OTA	operational transconductance amplifier
PCB	printed circuit board
PCE	power conversion efficiency
PM	phase margin
pMOS	p-channel MOS
PMS	Power Management System
PRU	Power Receiving Unit
PSSR	power supply rejection ratio
PTAT	proportional to absolute temperature
PTU	Power Transfer Unit
PVT	process voltage temperature

SMD Surface Mounted Device

SMPS switch mode power supply

SRF Self Resonance Frequency

TC temperature coefficient

UGF unity gain frequency

VCE voltage conversion efficiency

V_p peak voltage

V_{pp} peak to peak voltage

V_{tn} threshold voltage of n-channel MOS

V_{tp} threshold voltage of p-channel MOS

WPT Wireless Power Transfer